Two-phase, mass-transport model for direct methanol fuel cells with effect of non-equilibrium evaporation and condensation

W.W. Yang, T.S. Zhao *

Department of Mechanical Engineering, The Hong Kong University of Science and Technology, Clear Water Bay, Kowloon, Hong Kong SAR, China

Abstract

A two-phase, mass-transport model for liquid-feed direct methanol fuel cells (DMFCs) is developed by taking into account the effect of non-equilibrium evaporation and condensation of methanol and water. The comparison between the present model and other models indicates that the present model yields more reasonable predictions of cell performance. Particularly, it is shown that the models that invoke a thermodynamic-equilibrium assumption between phases will overestimate mass-transport rates of methanol and water, thereby resulting in an inaccurate prediction of cell performance. The parametric study using the present model reveals that the gas coverage at the flow channel–diffusion-layer interface is directly related to the gas-void fraction inside the anode porous region; increasing the gas-void fraction will increase the mass-transfer resistance of methanol and thus lower cell performance. The effects of the geometric dimensions of the cell structure, such as channel width and rib width, on cell performance are also investigated with the model developed in this work.
© 2007 Elsevier B.V. All rights reserved.

Keywords: Direct methanol fuel cell; Two-phase model; Mass transport; Methanol crossover; Parametric study

1. Introduction

The direct methanol fuel cell (DMFC) has been regarded as an attractive power source for portable and microelectronic devices because of its high efficiency, high specific energy, low emissions, and simple structure [1]. Nevertheless, widespread commercialization of DMFC technology is still hindered by several technological challenges, such as the low rate of the methanol oxidation reaction (MOR) on the anode, and mixed overpotential caused by methanol crossover to the cathode. In addition, coupled electrochemical reactions and transport of different species, e.g., reactants, products, electrons, protons and heat, make it difficult to achieve optimum design and operation of the DMFC. In an effort to resolve these challenging problems, mathematical modelling of the DMFC system plays an important role, as it can provide a powerful and economical tool to analyze the complex transport processes, which are rather difficult to be studied experimentally. Most of the previous fuel cell models have been based on the single-phase flow approach [2–17], which is apparently unrealistic because the coexisting liquid and gas flow behaviour has a significant influence on the mass-transport processes, as revealed by in situ flow visualization studies on DMFCs [18–20].

Although more realistic, the development of a two-phase, mass-transport model for the DMFC is rather challenging because of the complexity of two-phase flows. Murgia et al. [21] presented a one-dimensional model based on phenomenological transport equations for the DMFC. In order to consider two-phase flow interaction in the diffusion layer, they introduced a Gaussian function as an approximate representation of influence of the capillary pressure on the effective gas porosity. Wang and Wang [22] modelled the DMFC using the mixture multiphase flow model, in which the species in the liquid and gas phase are assumed to be in thermodynamic equilibrium. Birgersson et al. [23] studied numerically the anode mass transport in two-phase flow in a two-dimensional domain using the mathematical model developed by Wang and Wang [22]. Divisek et al. [24] presented a two-dimensional, two-phase model for the DMFC with the computational domain restricted to the

Nomenclature

A_{lg}	interfacial specific area between liquid and gas phase ($m^2\,m^{-3}$)
A_v	specific area ($m^2\,m^{-3}$)
C	molar concentration ($mol\,m^{-3}$)
D	diffusivity ($m^2\,s^{-1}$)
F	Faraday constant (96,478 $C\,mol^{-1}$)
$\mathbf{I}$	current vector ($A\,m^{-2}$)
I	current density ($A\,m^{-2}$)
I_{Cell}	cell current density ($A\,m^{-2}$)
I_p	parasitic current resulting from methanol crossover ($A\,m^{-2}$)
j_0	exchange current density ($A\,m^{-2}$)
j_a	anode current density ($A\,m^{-3}$)
j_c	cathode current density ($A\,m^{-3}$)
k_c	condensation rate ($mol\,atm^{-1}\,s^{-1}\,m^{-3}$)
k_e	evaporation rate (1 $atm^{-1}\,s^{-1}$)
k_H	Henry's law constant (Pa)
k_r	relative permeability
K	permeability of porous material (m^2)
$\dot{m}$	source term in mass conservation equation ($kg\,m^{-3}\,s^{-1}$)
M	molecular weight ($kg\,mol^{-1}$)
n_d	electro-osmotic drag coefficient
N	mol flux ($mol\,m^{-2}\,s^{-1}$)
p_c	capillary pressure (Pa)
p_g	gas-phase pressure (Pa)
p_l	liquid-phase pressure (Pa)
R	gas constant ($J\,mol^{-1}\,K^{-1}$)
$\dot{R}$	source term in species conservation equation ($mol\,m^{-3}\,s^{-1}$)
$\tilde{R}$	interfacial species transfer rate ($mol\,m^{-3}\,s^{-1}$)
$R_{contact}$	Ohmic contact resistance ($\Omega\,m^2$)
s	liquid saturation
T	temperature (K)
V_0	thermodynamic-equilibrium voltage (V)
V_{cell}	cell voltage (V)
x	coordinate, m, or mole fraction in liquid solution ($mol\,mol^{-1}$)
y	coordinate, m, or mole fraction in gas mixture ($mol\,mol^{-1}$)

Greek letters

α	gas-void fraction $(1-s)$
α_a	anode transfer coefficient at anode
α_c	cathode transfer coefficient at cathode
γ	reaction order of ORR
δ	thickness of porous layer (m)
ε	porosity of porous medium
η	overpotential (V)
θ_c	contact angle (°)
κ	ionic conductivity of membrane ($\Omega^{-1}\,m^{-1}$)
μ	viscosity ($kg\,m^{-1}\,s^{-1}$)

ρ	density ($kg\,m^{-3}$)
σ	interfacial tension ($N\,m^{-1}$)

Subscripts

A	anode
Acl	anode catalyst layer
Adl	anode diffusion layer
Afc	anode flow channel
C	cathode
Ccl	cathode catalyst layer
Cdl	cathode diffusion layer
Cfc	cathode flow channel
G	gas phase
L	liquid phase
Mem	membrane
M	methanol
MV	methanol vapour
W	water
WV	water vapour

Superscripts

eff	effective value
in	inlet condition
ref	reference value
sat	saturated value

membrane electrode assembly only. In their work, the presence of hydrophilic and hydrophobic pores was taken into account by introducing an experimental-data-fitted correction equation between capillary pressure and saturation, which was different from the Leverette function used in Ref. [22]. Although methanol permeation was considered, the mixed-potential effect was not addressed. Rice and Faghri [25] proposed a transient, multiphase model for a passive fuel-fed DMFC. The passive delivery system consisted of a porous material to deliver methanol to the fuel cell while controlling the concentration of methanol at the anode. This procedure allowed the rate of methanol crossover to be reduced. Noteworthy is that the evaporation/condensation of methanol and water was formulated in a manner to capture non-equilibrium effects between phases. This approach differed from the thermodynamic-equilibrium assumption employed elsewhere [22,23]. Recently, Liu and Wang [26] presented a two-phase model based on their earlier version [22], in which the catalyst layer was treated as a component, rather than an interface without thickness. In their DMFC model, however, the liquid and gas phase were assumed to be in thermodynamic equilibrium. Most recently, Yang and Zhao [27] presented a two-phase mass-transport model that was developed based on multiphase flow theory in a porous medium and hence there was no need to define the mixture pressure of the liquid and gas phases as in the multiphase mixture model. Another feature of the model was that the assumption of constant gas-phase pressure is eliminated. On the other hand, the model did not take into account the effect of methanol vapour transport.

The objective of this work is to extend the isothermal, two-phase, mass-transport model for DMFCs that has been developed earlier [27] by taking into account the effect of non-equilibrium evaporation and condensation between the phases. This new model enables removal of the assumption of a thermodynamic-equilibrium condition between the phases employed in previous models [22,23,26]. The model also eliminates the assumption of constant liquid pressure at the anode or constant gas-phase pressure at the cathode, as was adopted previously [28–30]. The mathematical model is presented and compared with other models. Finally, numerical results obtained from parametric studies by the model are presented and discussed.

2. Mathematical model

The two-dimensional domain, as sketched in Fig. 1, represents the typical geometry of a membrane electrode assembly (MEA) that consists of anode diffusion layer (ADL), an anode catalyst layer (ACL), a membrane (MEM), a cathode catalyst layer (CCL) and a cathode diffusion layer (CDL). The MEA is sandwiched between two parallel flow-field plates. Since both channel width and rib width in the parallel flow-field are symmetrical with respect to their middle point, only a half-rib width and a half-channel width need to be considered to save the computing time. As such, the computation domain is the region that is enclosed by the dashed lines.

2.1. Governing equations

We now present the governing equations for the two-dimensional, steady-state, two-phase mass transport in the DMFC anode and cathode porous regions. The model is developed based on our previous work [27], in which transport of methanol vapour and water vapour was not taken account. To consider the transport of these additional species with phase change, the effect of non-equilibrium evaporation and con-
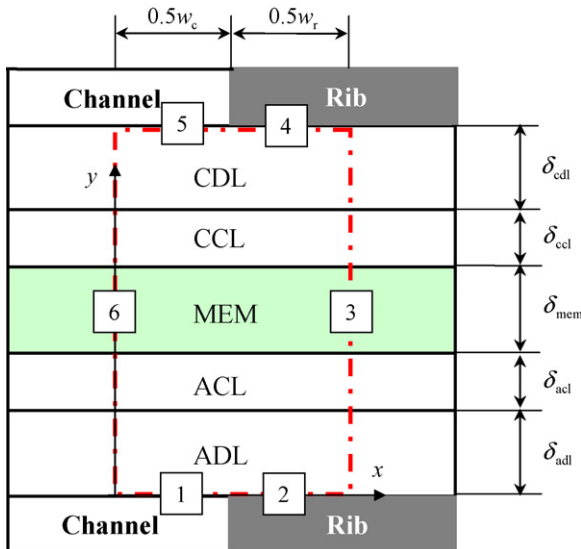
densation between the phases needs to be taken into account. This opposes the assumption of a thermodynamic equilibrium between the phases that was employed in previous models [22,23,26]. As such, in the anode and cathode porous region, a total of nine variables are involved. These includes the concentration of liquid methanol ($C_{M,l}$), the concentration of methanol vapour ($C_{MV,g}$), liquid water saturation in the anode ($s_{l,a}$), liquid pressure in the anode ($p_{l,a}$), the concentration of water vapour in the anode ($C_{WV,g,a}$), the concentration of gas oxygen in the cathode ($C_{O_2,g}$), liquid water saturation in the cathode ($s_{l,c}$), gas-phase pressure in the cathode ($p_{g,c}$), and the concentration of water vapour in the cathode ($C_{WV,g,c}$). Note that methanol vapour concentration, $C_{MV,g}$ and water vapour concentration, $C_{WV,g,a}$ are the two added variables compared with the previous model [27]. The governing equations that describe the mass conservation of each species in different phases are given below.

2.1.1. Anode porous region

$$C_{M,l} : \nabla \cdot \left[\left(-\frac{Kk_{rl}}{\mu_l} \nabla p_l \right) C_{M,l} - D_M^{eff} \nabla C_{M,l,a} \right] = \dot{R}_{M,l,a} \quad (1)$$

$$C_{MV,g} : \nabla \cdot \left[\left(-\frac{Kk_{rg}}{\mu_g} \nabla p_{g,a} \right) C_{MV,g,a} - D_{MV,g}^{eff} \nabla C_{MV,g,a} \right]$$
$$= \dot{R}_{MV,g,a} \quad (2)$$

$$s_{l,a} : \nabla \cdot \left[\left(-\frac{Kk_{rg}}{\mu_g/\rho_g} \right) \underbrace{\left(\frac{dp_c}{ds} \nabla s_{l,a} + \nabla p_{l,a} \right)}_{\nabla p_{g,a}} \right] = \dot{m}_{g,a} \quad (3)$$

$$p_{l,a} : \nabla \cdot \left[\left(-\frac{Kk_{rl}}{\mu_l/\rho_l} \nabla p_{l,a} \right) \right] = \dot{m}_{l,a} \quad (4)$$

$$C_{WV,g} : \nabla \cdot \left[\left(-\frac{Kk_{rg}}{\mu_g} \nabla p_{g,a} \right) C_{WV,g,a} - D_{WV,g}^{eff} \nabla C_{WV,g,a} \right]$$
$$= \dot{R}_{WV,g,a} \quad (5)$$

2.1.2. Cathode porous region

$$C_{O_2,g} : \nabla \cdot \left[\left(-\frac{Kk_{rg}}{\mu_g} \nabla p_{g,c} \right) C_{O_2,g,c} - D_{O_2,g}^{eff} \nabla C_{O_2,g,c} \right]$$
$$= \dot{R}_{O_2,g,c} \quad (6)$$

$$s_{l,c} : \nabla \cdot \left[\left(-\frac{Kk_{rl}}{\mu_l/\rho_l} \right) \underbrace{\left(-\frac{dp_c}{ds} \nabla s_{l,c} + \nabla p_{g,c} \right)}_{\nabla p_{l,c}} \right] = \dot{m}_{l,c} \quad (7)$$

$$p_{g,c} : \nabla \cdot \left[\left(-\frac{Kk_{rg}}{\mu_g/\rho_g} \right) \nabla p_{g,c} \right] = \dot{m}_{g,c} \quad (8)$$

Fig. 1. Schematic of model domain.

$$C_{WV,g,c} : \nabla \cdot \left[\left(-\frac{K k_{rg}}{\mu_g} \nabla p_{g,c} \right) C_{WV,g,c} - D^{eff}_{WV,g} \nabla C_{WV,g,c} \right]$$
$$= \dot{R}_{WV,g,c} \tag{9}$$

The interfacial transfer rates between liquid and vapour of methanol and water in the anode porous region are, respectively, by

$$\tilde{R}_M = A_{lg} h_{lg} s(1-s) \frac{p^{sat}_{MV} - p_{MV}}{RT} \tag{10}$$

and

$$\tilde{R}_w = \begin{cases} k_e \dfrac{\varepsilon s \rho_l}{M_{H_2O}} (y_{WV} p_g - p^{sat}_{WV}) & y_{WV} p_g < p^{sat}_{WV} \\ k_c \dfrac{\varepsilon (1-s) y_{WV}}{RT} (y_{WV} p_g - p^{sat}_{WV}) & y_{WV} p_g > p^{sat}_{WV} \end{cases} \tag{11}$$

where p^{sat}_{MV} and p^{sat}_{WV} denote the saturation pressure of methanol vapour and the saturation pressure of water vapour, respectively.

2.1.3. Membrane

Unlike in the anode porous region, only dissolved methanol and liquid water need to be considered, in the polymer electrolyte membrane as this is usually regarded as a gas insulator. Transport of methanol through membranes generally depends on molecular diffusion, electro-osmotic drag, and convection. Accordingly, the flux of methanol crossover (N_M) is given by

$$N_M = -D^{eff}_M \cdot \nabla C_M + n_{d,M} \frac{I}{F} - \left(\frac{K}{\mu_l} \frac{\Delta p_{l,c-a}}{\delta_{mem}} \right) C_M \tag{12}$$

With respect to the water transport, the flux due to diffusion mode can be ignored if the membrane is in equilibrium with liquid water on both sides. Hence, the flux of water crossover

(N_W) is given by

$$N_W = n_{d,H_2O} \frac{I}{F} - \frac{\rho_l}{M_{H_2O}} \frac{K}{\mu_l} \frac{\Delta p_{l,c-a}}{\delta_{mem}} \tag{13}$$

To make the above governing equations closed, some constitutive correlations and definitions are needed. These include capillary pressure, relative permeability for both gas and liquid phases, effective diffusion coefficients for each species, source terms and interfacial transfer rates of methanol and water between the phases. All these correlations and associated nomenclatures are listed in Table 1.

2.2. Boundary and interfacial conditions

As indicated in Fig. 1, the computational domain is enclosed by six boundaries. The conditions at each boundary are described below:

- *Boundary 1*: This boundary represents the inlet of reactant supply at the anode, at which the concentration of liquid methanol, liquid-phase pressure, liquid saturation and the concentrations of methanol vapour and water vapour are all specified to be inlet conditions:

$$C_{M,l} = C^{in}_M, \qquad C_{MV} = C^{in}_{MV}, \qquad C_{WV} = C^{in}_{WV},$$
$$p_l = p^{in}_l, \qquad s = 1 \tag{14}$$

- *Boundary 2*: This boundary is the interface between the anode diffusion layer and the anode rib collector, which is an impermeable wall. Accordingly, all the fluxes in the y direction are zero at this boundary:

$$\frac{\partial C_M}{\partial y} = 0, \qquad \frac{\partial C_{MV}}{\partial y} = 0, \qquad \frac{\partial C_{WV}}{\partial y} = 0,$$
$$\frac{\partial p_l}{\partial y} = 0, \qquad \frac{\partial s}{\partial y} = 0 \tag{15}$$

Table 1
Constitutive relations

Parameters	Expressions
Capillary pressure	$p_c = p_g - p_l = \sigma \cos\theta_c (\varepsilon/K)^{0.5} J(s)$, $J(s) = \begin{cases} 1.417(1-s) - 2.120(1-s)^2 + 1.263(1-s)^3, & 0 < \theta_c \leq 90° \\ 1.417s - 2.120s^2 + 1.263s^3, & 90° < \theta_c < 180° \end{cases}$
Relative permeabilities	$k_{rl} = s^3$ (liquid), $k_{rg} = (1-s)^3$ (gas)
Effective diffusion coefficients of species [27]	$D^{eff}_{i,g} = D_{i,g} \varepsilon^{1.5}(1-s)^{1.5}$　$(i : O_2, WV, MV)$,　$D^{eff}_M = \begin{cases} D_{M,l} \varepsilon^{1.5} s^{1.5}, & ADL \\ \dfrac{\varepsilon + \varepsilon_N}{\varepsilon/(D_{M,l}\varepsilon^{1.5}s^{1.5}) + \varepsilon_N/(D_{M,N}\varepsilon_N^{1.5})}, & ACL \\ D_{M,N}\varepsilon^{1.5}, & MEM \end{cases}$
General generation rate of mass in liquid phase	$\dot{m}_{l,a} = \begin{cases} -M_{H_2O}\tilde{R}_w - M_M\tilde{R}_M, & ADL \\ -(M_{H_2O} + M_M)\dfrac{j_a}{6F} - M_{H_2O}\tilde{R}_w - M_M\tilde{R}_M, & ACL \end{cases}$,　$\dot{m}_{l,c} = \begin{cases} -M_{H_2O}\tilde{R}_w, & CDL \\ M_{H_2O}\left(\dfrac{j_c}{2F} - \dfrac{I_p}{6F\delta_{ccl}}\right) - M_{H_2O}\tilde{R}_w, & CCL \end{cases}$
General generation rate of mass in gas phase	$\dot{m}_{g,a} = \begin{cases} M_{H_2O}\tilde{R}_w + M_M\tilde{R}_M & ADL \\ M_{CO_2}\dfrac{j_a}{6F} + M_{H_2O}\tilde{R}_w + M_M\tilde{R}_M & ACL \end{cases}$,　$\dot{m}_{g,c} = \begin{cases} M_{H_2O}\tilde{R}_w & CDL \\ -M_{O_2}\dfrac{j_c}{4F} + M_{CO_2}\dfrac{I_p}{6F\delta_{ccl}} + M_{H_2O}\tilde{R}_w & CCL \end{cases}$
Mole generation rate of species	$\dot{R}_{O_2} = \begin{cases} 0, & CDL \\ -\dfrac{j_c}{4F}, & CCL \end{cases}$,　$\dot{R}_{WV,c} = \begin{cases} \tilde{R}_w, & CDL \\ \tilde{R}_w, & CCL \end{cases}$,　$\dot{R}_{M,l} = \begin{cases} -\tilde{R}_M & ADL \\ -\dfrac{j_a}{6F} - \tilde{R}_M & ACL \end{cases}$,　$\dot{R}_{MV,a} = \begin{cases} \tilde{R}_M & ADL \\ \tilde{R}_M & ACL \end{cases}$,　$\dot{R}_{WV,a} = \begin{cases} \tilde{R}_W & ADL \\ \tilde{R}_W & ACL \end{cases}$

- *Boundary 4*: Similar to Boundary 2, Boundary 4 represents the cathode channel rib, at which all the fluxes in the y direction are zero:

$$\frac{\partial C_{O_2}}{\partial y} = 0, \quad \frac{\partial C_{WV}}{\partial y} = 0, \quad \frac{\partial p_g}{\partial y} = 0, \quad \frac{\partial s}{\partial y} = 0 \qquad (16)$$

- *Boundary 5*: This boundary represents the inlet of oxygen supply and the outlet of water removal at the cathode, at which the following boundary conditions are specified:

$$C_{O_2} = C_{O_2}^{in}, \quad C_{WV} = C_{WV}^{in}, \quad p_g = p_g^{in}, \quad s = 0 \qquad (17)$$

- *Boundaries 3 and 6*: These two boundaries are symmetrical, respectively, with respect to the middle point of the channel width and the middle point of the rib width. Hence, the gradients of all the variables in x direction are zero:

$$\frac{\partial C_M}{\partial x} = 0, \quad \frac{\partial C_{MV}}{\partial x} = 0, \quad \frac{\partial C_{O_2}}{\partial x} = 0, \quad \frac{\partial C_{WV}}{\partial x} = 0,$$

$$\frac{\partial p_l}{\partial x} = 0, \quad \frac{\partial p_g}{\partial x} = 0, \quad \frac{\partial s}{\partial x} = 0 \qquad (18)$$

The conditions at the interfaces between those functional layers in the 'sandwiched' cell are given based on the principle that the continuity and mass/species flux balance are required at each interface to satisfy the general mass and species conservation of the entire cell. More details can be found elsewhere [27].

2.3. Electrochemical kinetics

On the DMFC anode, the Tafel-like expression is used to model the methanol oxidation reaction (MOR) kinetics:

$$j_a = A_{v,a} j_{0,M}^{ref} \left(\frac{C_M}{C_M^{ref}} \right)^{\gamma} \exp \left(\frac{\alpha_a F}{RT} \eta_a \right) \qquad (19)$$

where the reaction order γ is related to the methanol concentration and is assumed to be zero-order when the methanol concentration is higher than a reference value. Otherwise, the first-order reaction is specified.

With respect to the electro-reduction reaction of oxygen on the cathode, modified first-order Tafel-like kinetics based on a liquid-film covered agglomerate model [27] is used, which gives

$$j_c = A_{v,c} j_{0,O_2}^{ref} \left(\frac{C_{O_2}/k_{H,O_2}}{C_{O_2}^{ref}} \right) \exp \left(\frac{\alpha_c F}{RT} \eta_c \right) \xi_1 \xi_2 \qquad (20)$$

where C_{O_2} represents oxygen concentration in the gas pores. Three factors k_{H,O_2}, ξ_1 and ξ_2 denote the Henry factor to capture the effect of dissolving process, the factor in view of the transfer resistance in liquid film and the factor in view of the transport resistance in the agglomerate, respectively.

2.4. Current balance and cell voltage

The protons and electrons produced by the MOR at the anode transfer to the cathode through the membrane and the external circuit, respectively. The cell current density can be calculated by

$$I_{Cell} = \frac{\iint_{ACL} j_a \, dx \, dy}{(w_c + w_r)/2} \qquad (21)$$

To account for methanol crossover, a 'parasitic' current density, I_p, is used to express the rate of methanol crossover:

$$I_p = \frac{6F \int_0^{(w_c+w_r)/2} N_M \, dx}{(w_c + w_r)/2} \qquad (22)$$

where the molar flux of methanol crossover, N_M, is given by Eq. (12).

At the cathode, it is assumed that both the cell current and the 'parasitic' current are entirely consumed by the oxygen reduction reaction (ORR), i.e.:

$$I_{Cell} + I_p = \frac{\iint_{CCL} j_c \, dx \, dy}{(w_c + w_r)/2} \qquad (23)$$

For a given anode overpotential, η_a, the cell current density, I_{Cell}, and the 'parasitic' current density can be determined from Eqs. (21) and (22), respectively. Then, the cathode mixed overpotential, η_c, with the effect of methanol crossover, can be obtained with the help of Eqs. (20) and (23). Finally, the cell voltage can be determined from:

$$V_{Cell} = V_0 - \eta_a - \eta_c - I_{Cell} \left(R_{contact} + \frac{\delta_{mem}}{\kappa} \right) \qquad (24)$$

where V_0, $R_{contact}$ and κ denote the thermodynamic-equilibrium voltage of a DMFC, the contact resistance and the proton conductivity of the membrane, respectively.

Table 2
Cell geometric dimensions and operating parameters

Parameters	Symbols	Values	Units
Anode diffusion layer thickness	δ_{adl}	2.6×10^{-4}	m
Anode catalyst layer thickness	δ_{acl}	0.2×10^{-4}	m
Membrane thickness (Nafion 115)	δ_{mem}	1.3×10^{-4}	m
Cathode diffusion layer thickness	δ_{cdl}	2.6×10^{-4}	m
Cathode catalyst layer thickness	δ_{ccl}	0.2×10^{-4}	m
Channel width	w_c	1.0×10^{-3}	m
Rib width	w_r	1.0×10^{-3}	m
Operation temperature	T	348.15	K
Anode inlet pressure	p_l^{in}	1.013×10^{-5}	Pa
Cathode inlet pressure	p_g^{in}	1.013×10^{-5}	Pa
Inlet methanol concentration at anode	C_M^{in}	1000	mol m^{-3}
Inlet methanol vapour concentration	C_{MV}^{in}	C_{MV}^{sat}	mol m^{-3}
Inlet oxygen concentration at cathode	$C_{O_2}^{in}$	7.35	mol m^{-3}
Inlet water vapour concentration at anode	C_{WV}^{in}	C_{WV}^{sat}	mol m^{-3}
Inlet water vapour concentration at cathode	C_{WV}^{in}	0	mol m^{-3}
Inlet liquid saturation at anode	s^{in}	1	
Inlet liquid saturation at cathode	s^{in}	0	

3. Results and discussion

The above-described governing equations for the cell geometric dimensions and operating parameters listed in Table 2 subjected to the boundary conditions, along with the constitutive relations shown in Table 1 and electrochemical properties listed in Table 3, are solved numerically using a self-written code, which was developed based on the SIMPLE algorithm with the finite-volume-method [27].

3.1. Model comparison

In this section, the cell performance predicated by the present model is compared with those predicated by other models. The predicted polarization curves at the same operating conditions are compared in Fig. 2, where Curve A corresponds to the present model, in which transport of methanol in both the liquid and
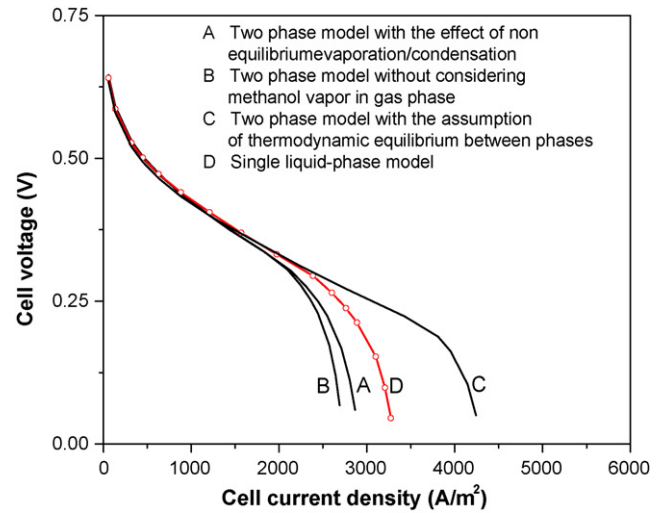
Fig. 2. Polarization curves predicted by different models with 1.0-M methanol operation.

Table 3
Physicochemical properties

Parameters	Symbols	Values	References
Porosity, permeability			
ADL	$\varepsilon_{adl}, K_{adl}$ (m^2)	0.7, 2.0×10^{-12}	[17]
ACL	$\varepsilon_{acl}, K_{acl}$ (m^2)	0.3, 1.0×10^{-14}	
MEM	$\varepsilon_{mem}, K_{mem}$ (m^2)	0.3, 2.0×10^{-18}	
CCL	$\varepsilon_{ccl}, K_{ccl}$ (m^2)	0.3, 1.0×10^{-14}	
CDL	$\varepsilon_{cdl}, K_{cdl}$ (m^2)	0.7, 2.0×10^{-12}	[17]
Nafion volume fraction			
ACL	$\varepsilon_{N,acl}$	0.4	
CCL	$\varepsilon_{N,ccl}$	0.4	
Diffusivities			
MeOH in water	$D_{M,l}$ (m^2 s^{-1})	6.69×10^{-9}	[23]
MeOH in Nafion	$D_{M,N}$ (m^2 s^{-1})	$4.9 \times 10^{-10} e^{[2436((1/333)-(1/T))]}$	[32]
Methanol vapour	$D_{M,g}$ (m^2 s^{-1})	$-6.954 \times 10^{-6} + 4.5986 \times 10^{-8}T + 9.4979 \times 10^{-11}T^2$	[22]
O$_2$ in gas	$D_{O_2,g}$ (m^2 s^{-1})	$1.775 \times 10^{-5}(T/273.15)^{1.823}$	[22]
O$_2$ in water	$D_{O_2,l}$ (m^2 s^{-1})	3.032×10^{-9}	[33]
O$_2$ in Nafion	$D_{O_2,N}$ (m^2 s^{-1})	1.844×10^{-10}	[33]
Water vapour	$D_{WV,g}$ (m^2 s^{-1})	$2.56 \times 10^{-5}(T/307.15)^{2.334}$	[22]
Viscosity of gas phase	μ_g (kg m^{-1} s^{-1})	2.03×10^{-5}	[36]
Viscosity of liquid phase	μ_l (kg m^{-1} s^{-1})	4.05×10^{-4}	[38]
Electro-osmotic drag coefficients of water and methanol	n_{d,H_2O}	2.5	[34]
	$n_{d,M}$	$n_{d,H_2O} x_M$	[34]
Evaporation rate constant for water	k_e (atm^{-1} s^{-1})	5.0×10^{-3}	[21]
Condensation rate constant for water	k_c (mol atm^{-1} s^{-1} cm^{-3})	5.0×10^{-5}	[21]
Interfacial transfer rate constant for methanol	h_{lg} (m^2 s^{-1})	0.001	[24]
Specific interfacial area between liquid and gas	A_{lg} (m^{-1})	10^5	[24]
Proton conductivity in membrane	κ (Ω^{-1} m^{-1})	$7.3 \, e^{[1268((1/298)-(1/T))]}$	[32]
Henry law constant for oxygen	k_{H,O_2}	$e^{((-666/T)+14.1)}/(RT)$	[33]
Henry law constant for methanol	$k_{H,M}$ (atm)	$0.096 \, e^{0.04511(T-273)}$	[22]
Saturation pressure of water vapour	$\log_{10} p_{WV}^{sat}$ (atm)	$-2.1794 + 0.02953(T-273 - 9.1837 \times 10^{-5}(T-273)^2$	[35]
		$+ 1.4454 \times 10^{-7}(T-273)^3$	
Saturation pressure of methanol vapour	p_{MV}^{sat} (atm)	$k_{H,M} x_{M,l}$	[22]
Thermodynamic voltage	V_0 (V)	1.21	[22]
Transfer coefficient of anode	α_a	0.5	[21]
Transfer coefficient of cathode	α_c	1.0	[37]
Anode exchange current density	$A_{v,a} j_{0,M}^{ref}$ (A m^{-3})	1.0×10^5	[27]
Cathode exchange current density	$A_{v,c} j_{0,O_2}^{ref}$ (A m^{-3})	1.14×10^3	[27]
Anode reference concentration	C_M^{ref} (mol m^{-3})	100	[22]
Cathode reference concentration	$C_{O_2}^{ref}$ (mol m^{-3})	0.52	[27]

vapour phases is considered and the effect of non-equilibrium evaporation and condensation is taken into account to deal with the transfer of interfacial species between the phases; Curve B corresponds to the model presented in Ref. [27], in which the mass transport of liquid methanol and gas carbon dioxide (CO_2) is considered, but methanol vapour in the gas phase is ignored; Curve C corresponds to the case predicted by the present model, but in which the local thermodynamic equilibrium between the phases is assumed. Note that this assumption is widely used in a number of fuel cell models reported earlier [22,23,26]. With the assumption, the gas phase in the anode can be treated to be saturated with methanol vapour. The details of the model for Curve C are presented in Appendix A. Curve D corresponds to the single-phase model, in which mass transport in the anode is modelled as a pure liquid flow, while in the cathode a pure gas flow is assumed. A comparison between Curves A and B indicates that the limiting current density predicted by the present model is slightly higher than that by the one without considering the mass transport of methanol vapour. Physically, this means that the added mass transport of methanol vapour tends to increase the overall concentration of methanol in the anode catalyst layer, and leads to a higher limiting current density [22]. Hence, ignoring the mass transport of methanol vapour will underestimate the cell performance.

For the same reason that methanol vapour phase is also considered in predicting Curve C, the limiting current density in Curve C is also higher than that in Curve B. However, a rather large difference can be found when a comparison is made between Curves A and C despite the fact that the transport of methanol vapour is considered in both corresponding models. This difference is attributed mainly to the fact that the model in predicting Curve A takes account of the effect of non-equilibrium evaporation and condensation, whereas the one in predicating Curve C has the assumption of a local thermodynamic equilibrium between the phases.

To illustrate which model gives a more realistic prediction, Curves A and C are now compared with Curved D, which is predicted by a single-phase model. As shown in Fig. 2, the limiting current density in Curve C is much higher than that in Curve D. However, the study has shown that the single-phase model over-predicts cell performance, because the presence of gas bubbles in the anode porous region and in the flow channel increases the resistance of methanol transfer to the catalyst layer and thereby results in an increase in mass-transport polarization [20,39]. Therefore, the models that have the thermodynamic-equilibrium assumption may overestimate the two-phase mass transport to give an unreasonable prediction of cell performance. By contrast, it is seen from Fig. 2 that the limiting current density in Curve A is smaller than that in Curve D, meaning that the present model with the effect of non-equilibrium evaporation and condensation gives a more realistic prediction of cell performance. In the following sections, all the results to be reported are predicted by the present model with the effect of non-equilibrium evaporation and condensation.

3.2. Velocity field and concentration distributions of methanol at different phases

To illustrate the liquid–gas two-phase flow behaviour, the velocity fields for both liquid and gas phases are shown in Fig. 3. As shown in Fig. 3a, the liquid phase moves from the anode channel to the catalyst layer as the result of the water and methanol consumption by the MOR and by the water and methanol crossover through the membrane to the cathode. By contrast, Fig. 3b shows that the gas phase in the anode porous region moves in the opposite direction of the liquid phase, as CO_2 is generated in the catalyst layer and moves towards the flow channel region. The liquid–gas two-phase counter-flow behaviour in the anode porous region shown in Fig. 3 illustrates the complexity in simultaneously transporting the reactants (methanol and water) towards the catalyst layer and removing the product (CO_2) from the porous region.

In order to indicate the two-phase mass-transport behaviour in the DMFC anode, the distribution of liquid methanol concentration, methanol vapour concentration and gas-void fraction are depicted in Fig. 4. Clearly, as shown in Fig. 4a, methanol concentration is highest at the anode-channel–diffusion-layer interface, and then decreases from the region near the rib region and in the catalyst layer as the result of mass-transfer resistance and mass consumption by the MOR in the catalyst layer. The gradient of methanol concentration implicitly indicates the diffusive transport of methanol, while the motion of liquid in porous anode as shown in Fig. 3a implies the convective transport of methanol. As a result, the transport of methanol in the liquid phase is determined by the superposition of two mechanisms: molecular diffusion and macroscopic convection.

The distribution of the methanol vapour concentration is presented in Fig. 4b. The concentration is higher near the channel
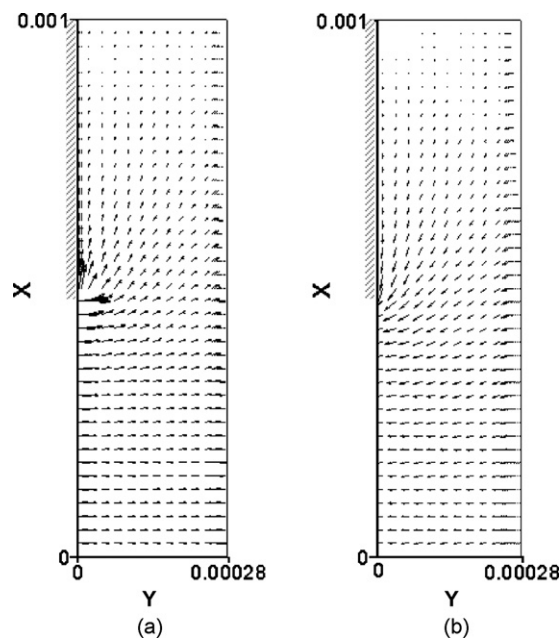

Fig. 3. Distributions of velocity vector of (a) liquid and (b) gas anode porous region (anode overpotential: 0.5 V).
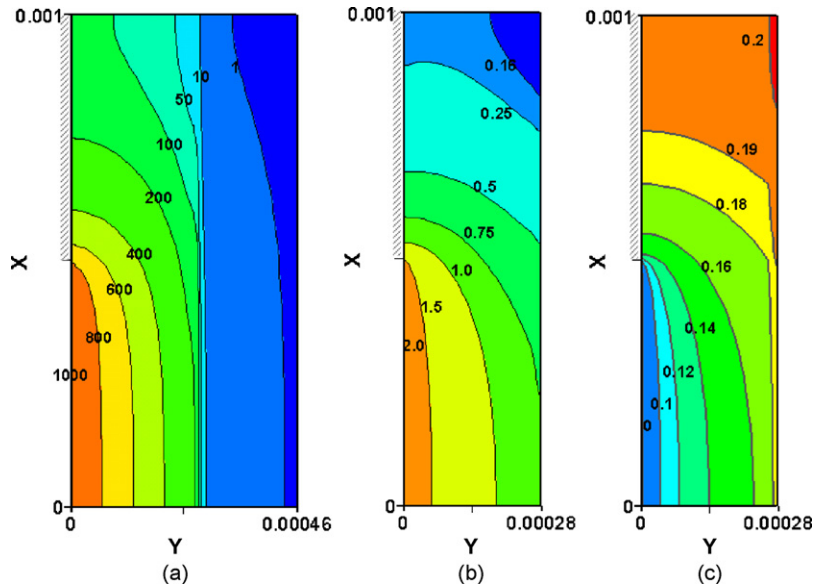
Fig. 4. Distributions of (a) methanol concentration in liquid phase through anode electrode and membrane, (b) methanol vapour concentration in gas phase and (c) gas-void fraction in anode porous region (anode overpotential: 0.5 V).

region and becomes lower in the catalyst layer as the result of the MOR there. Fig. 4c gives the distribution of the gas-void fraction, α, in the anode porous region. (Note that the value of α is obtained by subtracting liquid saturation from unity.) Clearly, the gas coverage level is higher in the region close to the catalyst layer than in the region close to the channel due to the generation of CO_2 as the result of the MOR in the catalyst layer. Moreover, the gas tends to accumulate in the impermeable region under the rib and this results to a higher level of gas coverage in the region under the rib. An increase in gas coverage in the porous medium will reduce the space available for methanol solution, which, in turn, will lead to an increase in the mass-transfer resistance of methanol from the channel to the reaction catalyst layer.

3.3. Analysis of mass transport of methanol

Next, we consider the two-phase mass transport of methanol in the DMFC anode. The total flux of methanol in the anode diffusion layer is comprised of two contributions, namely: methanol transport in a liquid solution and methanol vapour transport in the gas phase. The variation in current density in the catalyst layer along the channel and rib width (x direction in Fig. 2) for three different cases is shown in Fig. 5. Case A corresponds to the model that only considers methanol diffusive transport in a liquid phase; Case B considers methanol diffusion and convection transport in the liquid phase; and Case C corresponds to the model that considers methanol diffusion and convection in both the liquid phase and the gas phase. From Fig. 5, clearly, the current density for Case C is higher that for Case B owing to the contribution of methanol vapour transport in the gas phase. It also can be seen that the current density for Case B is a slightly higher than the value for Case A due to the fact that the convective motion of liquid solution tends to decrease the resistance of methanol transport to the catalyst layer, as discussed earlier.

The limiting current density corresponding to the mass-transport limitation of methanol as the result of each of the three transport mechanisms, A–C, is shown in Fig. 6 for 0.5, 0.75 and 1 M methanol feeding concentrations. Note that in Fig. 6 the scale of the limiting current density was set to begin with $1000\,A\,m^{-2}$ to give prominence to the differences between Cases A–C. It should be recognized that the difference in the limiting current density between Cases C and B corresponds to the mass flux of methanol due to transport in the vapour phase, designated by I; the difference between Cases B and A corresponds to the mass flux of methanol due to convection in liquid phase, designated by II; and III in Fig. 6 represents the mass flux of methanol due to diffusion in liquid phase, i.e., Case A. As can be seen from Fig. 6, for a 1.0 M methanol feeding con-
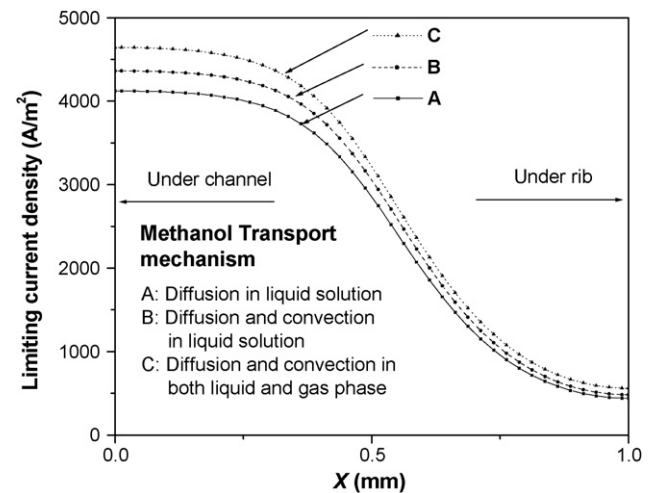

Fig. 5. Limiting current densities corresponding to mass flux of methanol as result of (A) methanol diffusion in liquid solution only; (B) methanol diffusion and convection in liquid solution; (C) methanol diffusion and convection in both liquid and gas phase.
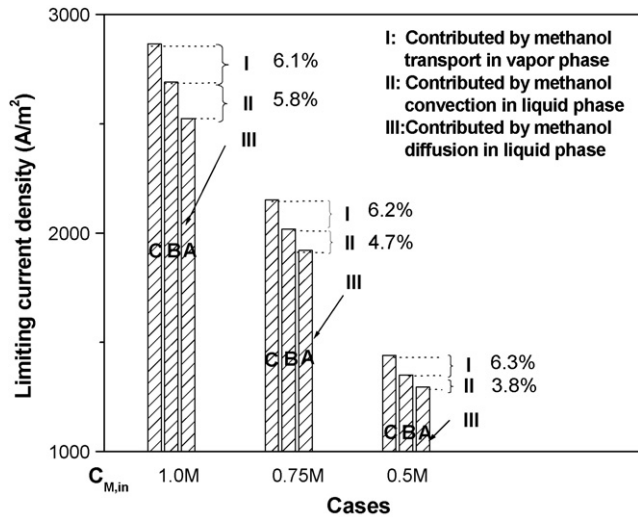
Fig. 6. Limiting current densities corresponding to mass flux of methanol as result of different transport mechanisms for different methanol concentrations.

centration, the contribution by methanol transport in the vapour phase and methanol convective transport in the liquid phase, respectively, take about 6% of the total limiting current density. The rest 88% is contributed by methanol diffusive transport in the liquid phase. For all the cases studied, the results indicate that the mass flux of methanol is predominated by the methanol diffusion in the liquid phase. Methanol convection in the liquid phase and methanol vapour transport in the gas phase only contribute a relatively small portion of the total mass flux. However, it should be pointed out that the results presented in Fig. 6 were obtained for a DMFC with a parallel flow-field, in which the convective motion of liquid is relatively weaker. For a ser-

pentine flow-field, however, the pressure difference between the two adjacent channels will force the liquid convection through the diffusion layer and this induces stronger forced-convection [17,31]. As a result, methanol convection in the liquid phase may become more important than methanol diffusion in the liquid phase.

Another point that should be mentioned about the results in Fig. 6 is that methanol vapour transport in the gas phase is influenced by the total gas-void fraction in the porous region. In this study, the gas-void fraction in the anode porous region, as shown in Fig. 3c, is relatively small because of the assumption that no gas covers the anode-channel–diffusion-layer interface. This assumption can be justified only when gas bubbles in the anode channel are removed quickly by the high-speed liquid flow. Otherwise, coverage of the interface with gas bubbles will result in a much higher gas-void fraction inside the diffusion layer and the catalyst layer. As a result, the contribution of methanol vapour transport in the gas phase will play an important role. The influence of the interfacial gas coverage will be discussed in the following section.

3.4. Effect of gas coverage level at the anode-channel–diffusion-layer interface

In the DMFC anode, it is understood that the presence of gas bubbles accumulated in the flow channel will reduce the contact surface area between the liquid methanol and diffusion layer, thus blocking methanol transfer from the channel to the diffusion layer. Fig. 7 shows the distribution of the gas-void fraction in the porous anode when the interfacial gas coverage level is at $\alpha = 0.2$, 0.4 and 0.6. Generally, the gas-void fraction is higher in the region close to the catalyst layer and in the
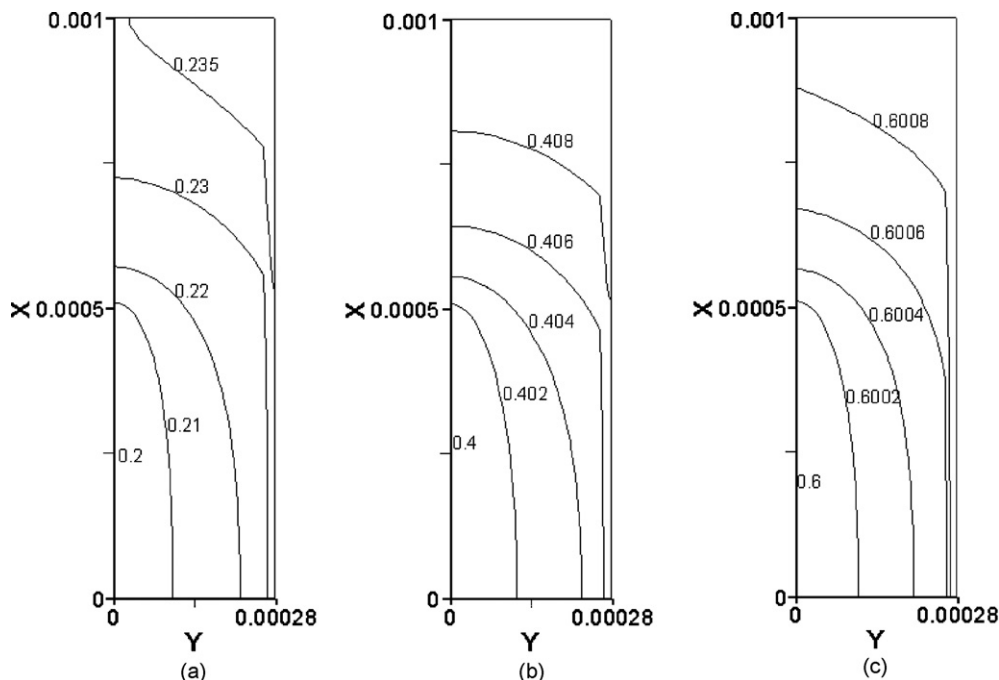

Fig. 7. Distributions of gas-void fraction in anode porous region for different interfacial gas coverage levels: (a) $\alpha_{AFC/ADL} = 0.2$; (b) $\alpha_{AFC/ADL} = 0.4$; and (c) $\alpha_{AFC/ADL} = 0.6$ (methanol concentration: 1 M; anode overpotential: 0.5 V).
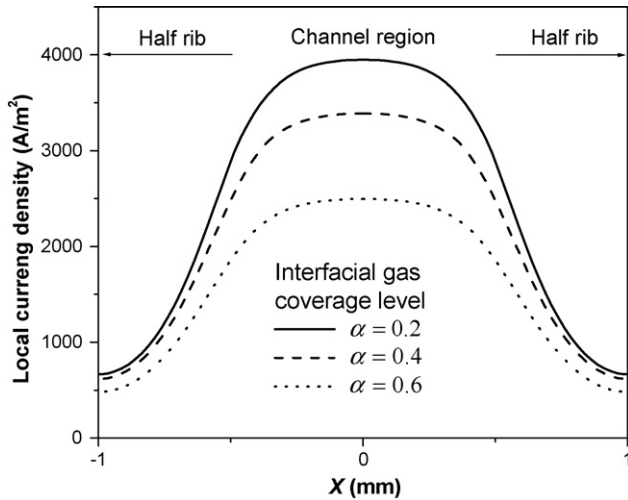
Fig. 8. Distributions of local current density along channel and rib width for different interfacial gas coverage levels (methanol concentration: 1.0 M; anode overpotential: 0.5 V).

region under the rib than in the region close to the flow channel. It can be seen that the overall gas-void fraction increases with increasing gas coverage level at the interface. This result explains why accumulation of gas at the AFC–ADL interface hinders the product gas CO_2 moving out of the diffusion layer and results in accumulation of gas bubbles in the porous region.

The variation in the local current density along the channel width and the rib width for different interfacial gas coverage levels is presented in Fig. 8. It is clear that the overall local current density is lowered with an increasing level of interfacial gas coverage. The effect of the degree of interfacial gas coverage on cell performance is presented in Fig. 9. As can be seen, the limiting current density decreases with increasing the interfacial gas coverage. It is worth mentioning that, in practice, the level of interfacial gas coverage cannot be arbitrarily specified, as it is influenced by many factors such as the anode flow rate, the geometry of flow channel, and the interfacial properties of the
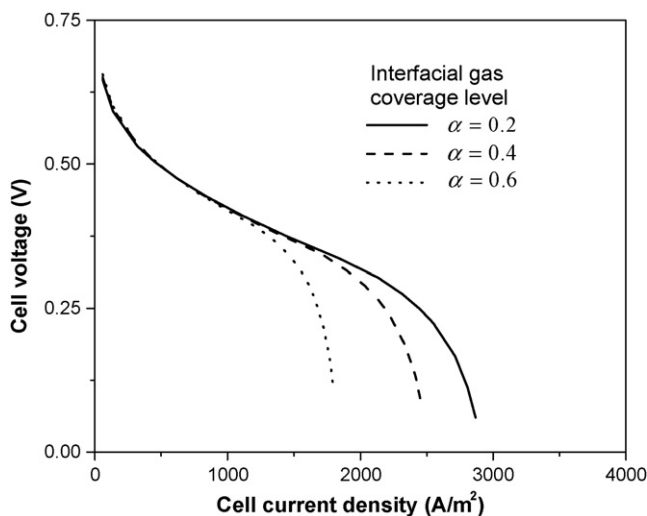
gas-diffusion layer. Moreover, the extent of interfacial gas coverage also varies along the flow direction due to the accumulation of gas along the channel.

3.5. Effect of cell dimensions

The mass transport inside the DMFC is influenced by many parameters of the structural details, such as the channel width (w_{ch}) and the channel-to-rib width ratio (C/R). In order to improve cell performance, it is essential to understand the parametric effects on two-phase mass transport and cell performance.

3.5.1. Effect of channel width

To study the effect of channel width, the C/R ratio was fixed at unity. It is should be recognized that reducing the channel width while fixing the C/R ratio is equivalent to having more channels in the parallel flow-field. The distribution of the gas-void fraction and the methanol concentration at the ADL–ACL interface along the channel and the rib width (in the dimensionless form, $X = x/w_{ch}$) for different channel widths is presented in Fig. 10. As shown in Fig. 10a, the overall level of the gas-void fraction at the ADL–ACL interface decreases and becomes a more uniform distribution as the channel and rib widths decrease. It is understood that the produced CO_2 in the region under the rib has to be transported across the thickness of the ADL and the width of the rib to the channel. When the channel and the rib widths decrease while the thickness of the diffusion layer does not change, the shorter width of rib assists removal of the gas in the region under the rib. This explains why significant changes in the gas coverage level occur in the region under the rib as the rib width changes. By contrast, only small changes are observed in the regions under the channel. The decrease in gas coverage results in a larger area for the transport of methanol solution. It is seen in Fig. 10b that the overall methanol concentration is more uniform and higher for a smaller rib width as the result of the short transfer distance from the channel to the region

Fig. 9. Effect of interfacial gas coverage on cell performance with 1.0 M methanol operation.
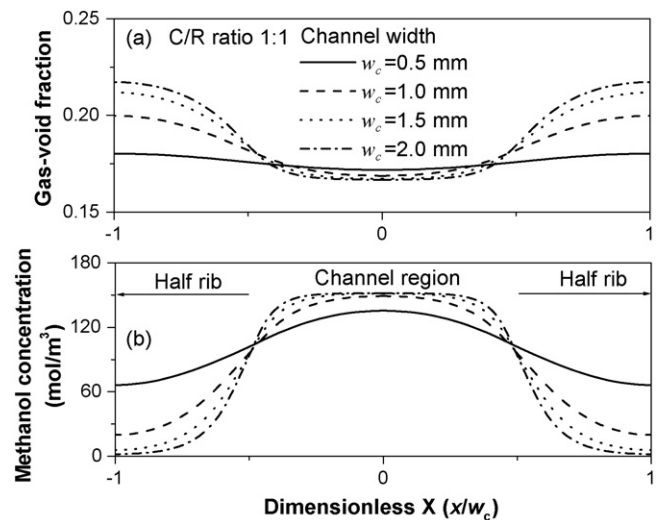

Fig. 10. Distributions of (a) gas-void fraction and (b) methanol concentration at ADL–ACL interface for various channel widths (methanol concentration: 1.0 M; anode overpotential: 0.5 V).

under the rib and decreased gas blockage. The uniform distribution of methanol in the catalyst layer is favourable for sufficient utilization of the MEA area under the rib region.

Reducing the channel and the rib width leads to higher methanol concentration and lower gas coverage in the region under the rib, resulting in higher and more uniform current density distribution. As a result, the limiting current density of the cell increases, as can be seen in Fig. 11. It must be pointed out that although a smaller channel is preferred if the C/R ratio is constant, one has to consider the fact that a smaller channel width may result in a higher flow resistance in the channel. Moreover, a smaller channel may also result in transient gas bubble hold-up in the flow channels, thereby severely blocking the methanol supply [20].

3.5.2. Effect of channel-to-rib width ratio

The effect of the C/R ratio is studied by keeping the total width of the channel and the rib constant. The distributions of local gas-void fraction and methanol concentration at the ADL–ACL interface for different C/R ratios are shown in Fig. 12. As the C/R ratio increases, the overall gas-void fraction decreases and becomes more uniform due to the decrease in transport distance for gas removal under the rib, which thus offers more transfer space for methanol solution. Accordingly, the methanol concentration increases and becomes more uniform in distribution with increasing C/R ratio, as shown in Fig. 12b. The results indicate that a larger C/R ratio leaves a larger accessible catalyst area and also improves the removal of products, resulting in a more uniform distribution of reactants and a more effective utilization of the MEA surface.

The effect of the C/R ratio on cell performance is presented in Fig. 13. The results show that the limiting current density increases with increasing C/R ratio, due mainly to the increased transfer area exposed to the open channel. It should be recognized, however, that an increasing C/R ratio may lead to a decrease in the contact area between the rib and electrode and the electron collector which, in turn, may cause an increase in cell
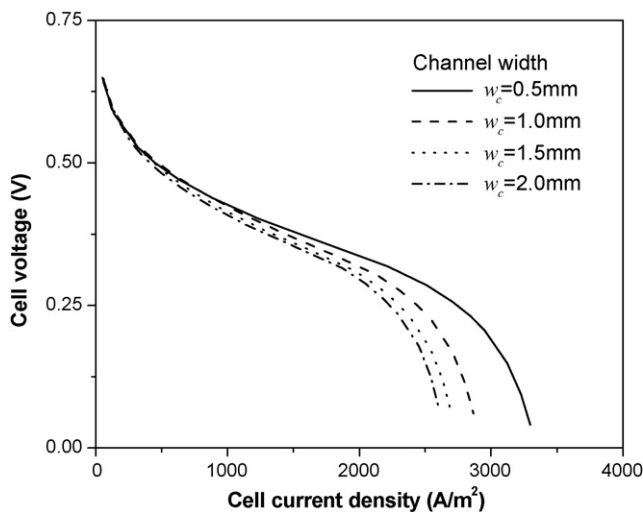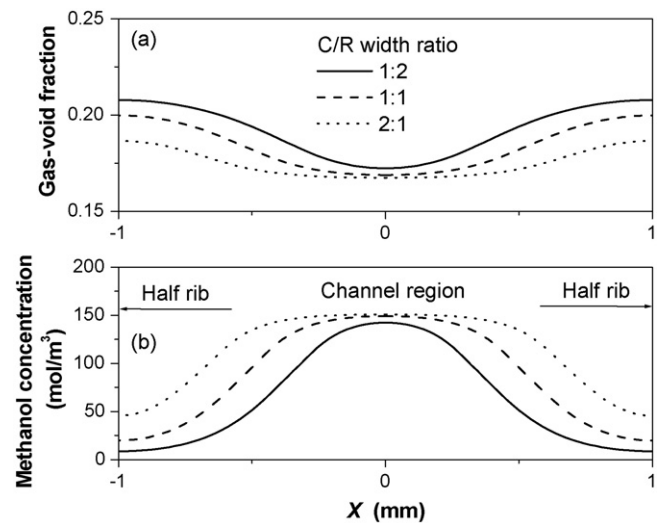

Fig. 12. Distributions of (a) gas-void fraction and (b) methanol concentration at ADL–ACL interface for different C/R ratio (anode overpotential: 0.5 V).
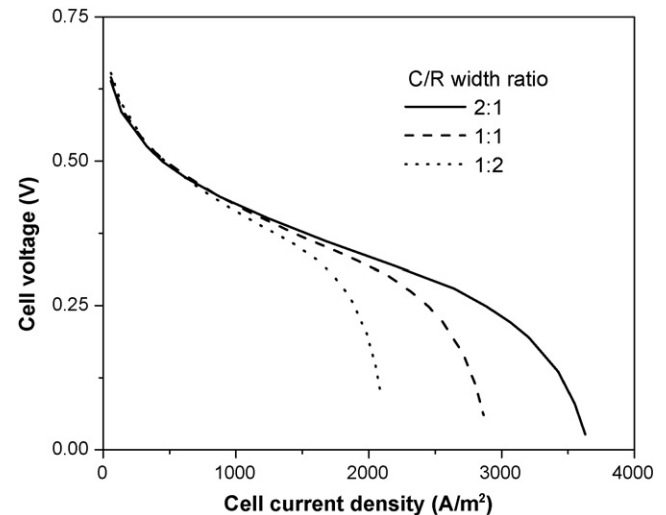

Fig. 13. Effect of channel-to-rib width ratio on cell performance (methanol concentration: 1.0 M).

internal resistance. A larger C/R ratio also means that electrons have to transfer over a longer distance at the in-plane direction in the diffusion layer to the current-collector, resulting in a larger Ohmic loss. This aspect must be taken into consideration in the optimum design of the DMFC.

4. Conclusions

In this work, a two-phase mass-transport model for a liquid-feed DMFC has been developed. It considers the transport of methanol/methanol vapour, and water/water vapour at the anode, and the transport of oxygen at the cathode. In particular, the model takes into account the effect of non-equilibrium evaporation and condensation, which eliminates the thermodynamic-equilibrium assumption employed in other previous two-phase mass-transport models. It has been shown that the thermodynamic-equilibrium assumption between liquid and

Fig. 11. Effect of channel width on cell performance (methanol concentration: 1.0 M).

vapour phases will lead to an unreasonable prediction of cell performance. The parametric study using the model developed in this work indicates that: (1) the gas coverage at the anode-channel–diffusion-layer interface has a significant influence on the gas-void fraction inside the anode porous region, thereby increasing the mass-transfer resistance of methanol and lowering cell performance; (2) the geometric dimensions of the cell structure, including the rib width and channel-to-rib width ratio, greatly influence the uniformity of reactant distributions, the current density profile, and the overall cell performance.

Acknowledgement

Appendix A. The model with the assumption of thermodynamic equilibrium

The assumption that a local thermodynamic equilibrium prevails between the liquid and gas phases implies that

$$C_{MV,g} = \frac{p_{MV}^{sat}}{RT} \tag{a1}$$

where the methanol vapour pressure can be obtained by Henry's law:

$$p_{MV}^{sat} = k_{H,M} x_{M,1} \dot{=} k_{H,M} \frac{M_{H_2O}}{\rho_1} C_{M,1} \tag{a2}$$

The mass conservation of methanol can now be obtained by superposition of methanol transport in the liquid and gas phases to give

$$\nabla \cdot \left[\left(-\frac{K k_{rl}}{\mu_1} \nabla p_1 \right) C_{M,1} - D_M^{eff} \nabla C_{M,1,a} \right]$$
$$+ \nabla \cdot \left[\left(-\frac{K k_{rg}}{\mu_g} \nabla p_{g,a} \right) C_{MV,g,a} - D_{MV,g}^{eff} \nabla C_{MV,g,a} \right]$$
$$= \dot{R}_{M,1,a} + \dot{R}_{MV,g,a} \tag{a3}$$

Combining Eqs. (a1)–(a3), we obtain

$$\nabla \cdot \left\{ \left[\left(-\frac{K k_{rl}}{\mu_1} \right) \nabla p_{1,a} + \left(-\frac{K k_{rg}}{\mu_g} \right) \psi \nabla p_{g,a} \right] C_{M,1,a} \right.$$
$$\left. - (D_{M,1}^{eff} + D_{MV,g}^{eff} \psi) \nabla C_{M,1,a} \right\} = \dot{R}_{MOR} \tag{a4}$$

where the term $\dot{R}_{MOR}$ represents the molar consumption rate by the MOR in the anode catalyst layer only. Solving Eq. (a4), along with Eqs. (3)–(10), yields the results for the case in which

it is assumed there is thermodynamic equilibrium between the phases.

References

[1] C.K. Dyer, J. Power Sources 106 (2002) 31.
[2] S.F. Baxter, V.S. Battaglia, R.E. White, J. Electrochem. Soc. 146 (1999) 437.
[3] K. Scott, P. Argyropoulos, K. Sundmacher, J. Electroanal. Chem. 477 (1999) 97.
[4] P. Argyropoulos, K. Scott, A.K. Shukla, C. Jackson, J. Power Sources 123 (2003) 190.
[5] K.T. Jeng, C.W. Chen, J. Power Sources 112 (2002) 367.
[6] A.A. Kulikovsky, J. Electrochem. Soc. 152 (2005) A1121.
[7] A.A. Kulikovsky, Electrochem. Commun. 6 (2004) 1259.
[8] J.P. Meyers, J. Newman, J. Electrochem. Soc. 149 (2002) A710.
[9] J.P. Meyers, J. Newman, J. Electrochem. Soc. 149 (2002) A718.
[10] J.P. Meyers, J. Newman, J. Electrochem. Soc. 149 (2002) A729.
[11] E. Birgersson, J. Nordlund, H. Ekstrom, M. Vynnycky, G. Lindbergh, J. Electrochem. Soc. 150 (2003) A1368.
[12] J. Nordlund, G. Lindbergh, J. Electrochem. Soc. 149 (2002) A1107.
[13] H. Guo, C.F. Ma, Electrochem. Commun. 6 (2004) 306.
[14] A.A. Kulikovsky, J. Divisek, A.A. Kornyshev, J. Electrochem. Soc. 147 (2000) 953.
[15] J.B. Ge, H.T. Liu, J. Power Sources 160 (2006) 413.
[16] C.H. Chen, T.K. Yeh, J. Power Sources 160 (2006) 1131.
[17] Q. Ye, T.S. Zhao, C. Xu, Electrochim. Acta 51 (2006) 5420.
[18] H. Yang, T.S. Zhao, Q. Ye, J. Power Sources 139 (2005) 79.
[19] X.G. Yang, F.Y. Zhang, A.L. Lubawy, C.Y. Wang, Electrochem. Solid State Lett. 7 (2004) A408.
[20] C.W. Wong, T.S. Zhao, Q. Ye, J.G. Liu, J. Electrochem. Soc. 152 (2005) A1600.
[21] G. Murgia, L. Pisani, A.K. Shula, K. Scott, J. Electrochem. Soc. 150 (2003) A1231.
[22] Z.H. Wang, C.Y. Wang, J. Electrochem. Soc. 150 (2003) A508.
[23] E. Birgersson, J. Nordlund, M. Vynnycky, C. Picard, G. Lindbergh, J. Electrochem. Soc. 151 (2004) A2157.
[24] J. Divisek, J. Fuhrmann, K. Gartner, R. Jung, J. Electrochem. Soc. 150 (2003) A811.
[25] J. Rice, A. Faghri, Int. J. Heat Mass Trans. 49 (2006) 4804.
[26] W.P. Liu, C.Y. Wang, J. Electrochem. Soc. 154 (2007) B352.
[27] W.W. Yang, T.S. Zhao, Electrochim. Acta 52 (2007) 6125.
[28] D. Natarajan, T.V. Nguyen, J. Electrochem. Soc. 148 (2001) A1324.
[29] G.Y. Lin, W.S. He, T.V. Nguyen, J. Electrochem. Soc. 151 (2004) A1999.
[30] G.Y. Lin, T.V. Ngyyen, J. Electrochem. Soc. 153 (2006) A372.
[31] C. Xu, Y.L. He, T.S. Zhao, R. Chen, Q. Ye, J. Electrochem. Soc. 153 (2006) A1358.
[32] K. Scott, W.M. Taama, J. Cruichshank, J. Power Sources 65 (1997) 159.
[33] D. Song, Q. Wang, Z. Liu, T. Navessin, M. Eikerling, S. Holdcroft, J. Power Sources 126 (2004) 104.
[34] X. Ren, T.E. Springer, T.A. Zawodzinski, S. Gottesfeld, J. Electrochem. Soc. 147 (2000) 466.
[35] A. Kazim, H.T. Liu, P. Forges, J. Appl. Electrochem. 29 (1999) 1409.
[36] S. Um, C.Y. Wang, K.S. Chen, J. Electrochem. Soc. 147 (2000) 4485.
[37] Y. Wang, C.Y. Wang, J. Electrochem. Soc. 153 (2006) A1193.
[38] J.H. Nam, M. Kaviany, Int. J. Heat Mass Trans. 46 (2003) 4595.
[39] P. Argyropoulos, K. Scott, W.M. Taama, J. Appl. Electrochem. 29 (1999) 661.